DOI 10.1007/s11106-024-00419-3
Powder Metallurgy and Metal Ceramics, Vol. 62, Nos. 9-10, January, 2024 (Ukrainian Original Vol. 62, Nos. 9-10, Sept.-Oct., 2023)

STUDY OF GEOMETRIC PARAMETERS AND MECHANICAL PROPERTIES OF METAL-BASED COMPOSITES

T. Kulpinas,[1] R. Kandrotaitė Janutienė,[1,2] and O. Sizonenko[1]

UDC 621.762;669.295

As the aerospace industry continues to grow, so does the demand for new materials that can withstand high temperatures and corrosive environments. In this paper, materials from the Ti–Al–C system that thrives in the aforementioned environments are studied. The method of measuring the grain size was described according to the relevant standards. The geometrical parameters of titanium carbide and its volume fraction have been determined under the ASTM E112 and ASTM E562 standards, respectively, for two series of specimens that were produced with different parameters and methods. The grain sizes determined are G12 and G12.5 according to ASTM E112. The volume fractions determined for the two series of samples are 20.22 and 17.65%, respectively. Using the above parameters, elastic and shear modulus, and Poisson's ratio were determined for the specimens tested using RVE modeling. RVE results showed that materials with higher volume fractions and larger average grain size resulted in stiffer materials. Specimens with higher TiC content exhibited higher elastic and shear modules, which were 153.6 and 58.3 GPa, respectively. Poisson's ratio was the lowest at 0.315. However, the difference was not significant between the specimens, the elasticity and shear modulus, of a specimen with a lower concentration of TiC, are 145 and 55.2 GPa, respectively. Poisson's ratio was higher and equal to 0.319. Comparing the above properties with the popular aerospace alloy Ti–6Al–4V, both specimens are much stiffer.

Keywords: *metal-based composites, titanium, Ti–Al–C system, RVE, microstructure, grain size, volume fraction.*

INTRODUCTION

Titanium is the fourth most used structural element in the world after aluminum, magnesium, and iron. Despite its wide application, the price of titanium is high. This is due to the complex process of extracting the metal from the ore and transforming the ingot into a finished product [1]. Nevertheless, titanium and its alloys are used in aerospace applications, and the demand for them is growing. Figure 1 illustrates how titanium is used on Boeing airplanes. As shown in the chart, the use of titanium in airplanes is as high as 15%.

Titanium is being used more and more as composites become more prevalent in aircraft construction. The excellent compatibility of titanium with these composite materials [3] and other properties have led to its use with the proliferation of carbon fiber-reinforced plastics. Alloys of other metals are less compatible with carbon fiber-reinforced plastics due to galvanic corrosion.

[1]Kaunas University of Technology, Kaunas, Lithuania.
[2]To whom correspondence should be addressed; e-mail: raskand@ktu.lt.

Published in Poroshkova Metallurgiya, Vol. 62, Nos. 9–10 (553), pp. 99–118, 2023. Original article submitted October 7, 2023.

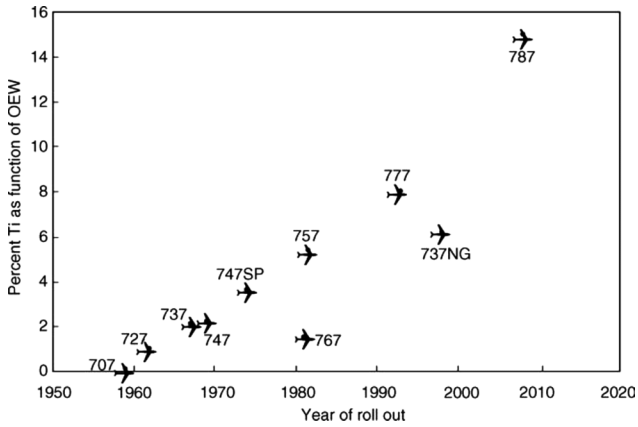

Fig. 1. Application of titanium on Boeing airplanes as a percentage of operating empty weight [2]

Titanium's properties have led to an increase in its use. These include:

- strength-to-weight ratio (titanium is as strong as steel, but approximately 45% lighter; also, titanium has the highest strength-to-weight ratio of any known metal [1]);
- corrosion resistance (the metal is completely covered with an oxide film that protects it from corrosion, scratches, and dents; excellent corrosion resistance results in lower maintenance and repair costs [4]);
- wide operating temperature range [4];
- resistance to cracking [4];
- excellent compatibility with carbon fiber-reinforced plastics widely used in aircraft (the coefficients of thermal expansion and corrosion resistance are similar [3]).

The application of composites in modern aircraft is at an all-time high. Figure 2 illustrates how composite materials are used in modern airplanes.

Composites and new materials have significantly improved performance, so the use of composites will likely grow as new materials are discovered.

Due to its high melting point, good thermal conductivity, low density, wear and corrosion resistance, and affordable price, Ti composites have become one of the most promising ultra-high temperature structural materials. For example, the three-layer carbide phases Ti_2AlC and Ti_3AlC_2 (MAX phases) show an ex-cellent combination of favorable ceramic and metallic properties [6, 7]. In contrast to conventional ceramic materials, these materials are also easily machined [8]. The crystal structure of MAX phases Ti_2AlC/Ti_3AlC_2 is hexagonal and is shown in Fig. 3.

Among the production methods for Ti–Al–C composites are high voltage electric discharge (HVED) and spark plasma sintering (SPS) processes [6]. HVED of titanium powder in hydrocarbon liquid is one of the most promising electric discharge methods for extracting submicro- and nanosized titanium carbide powder [10].

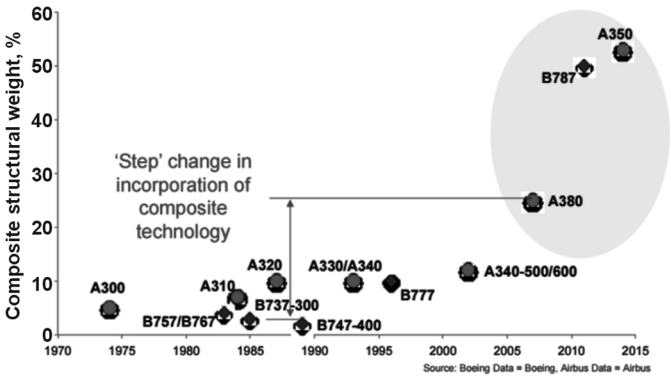

Fig. 2. Increased usage of composite structures in next-generation aircraft [5]

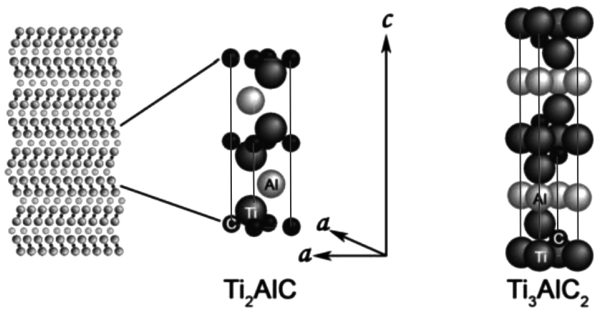

Fig. 3. Crystal structure of MAX phases Ti_2AlC/Ti_3AlC_2 [9]

TABLE 1. Effect of Grains Sizes of Commercially Pure Titanium on its Mechanical Properties [14]

Grain size, μm	Yield strength, MPa	Tensile strength, MPa	Relative elongation, %
4	381	450	0.133
10	310	405	0.127
50	249	268	0.113
1.9	525	605	0.021
3.2	505	575	0.041
5.1	483	556	0.05

HVED processing of metal powders leads to significantly better particle distribution and synthesis of refractory elements such as TiC, $AlTi_3$, AlTi, Al_2Ti, $AlTi_3$, as well as the synthesis of Ti_3AlC_2 and Ti_3AlC MAX phases [11, 12]. During the HVED process, the powder particles are subjected to mechanical and thermoelectric factors, resulting in their excellent dispersion. Hydrocarbon liquid prevents the particles from oxidizing, and the pyrolysis also creates conditions for the synthesis of carbides [12].

SPS is a process for baking powders under medium uniaxial pressure, up to 150 MPa, and high temperature, up to 2,500°C. The process is based on high-intensity, low-voltage alternating current. The temperature increases by 1,000°C per minute. SPS can achieve complete densification of ceramic or metal powders by rapid heating and cooling under uniaxial pressure. This results in successful sintering at temperatures lower than 200 to 500°C compared to conventional baking [13].

The grain size of sintered composites also affects the properties of these materials. Z.W. Huang, P.L. Yong, H. Zhou, and Y.S. Li investigated the effect of grain size on mechanical properties [14]. The results of this study are presented in Table 1. It can be seen from the table that the smaller the grains of the material, the stronger the material. The annealed samples became more ductile as the grain size decreased, but conversely, for the annealed and rolled samples, the material became less ductile after rolling even as the grain size increased. As the grain size decreased, the material also became harder. This study is evidence that grain size has an effect on the mechanical properties of the material, but it is not a complete description of the properties. H. Garbacza, P. Wiecińskib, D. Kuczyńskaa, D. Kubackaa, and K.J. Kurzydłowski established that grain size has an influence not only on mechanical properties but also on surface quality [15]. The grain size affected the structure of the titanium oxide film, which resulted in changing the adhesion properties of liquids. The roughness of the surface is also affected.

The ability of a crystalline material to undergo plastic deformation is dependent on the ability of the dislocations to move freely in the material. Grain boundaries are areas of excess molecules and an increased number of defects that do not belong to a symmetric crystal lattice. These defects in the crystal lattice impede the movement of dislocations through the material. Therefore, as the grain size decreases, we get more grain boundaries and material defects such as dislocations, and thus the material becomes stronger [16].

Thus, grain size has a measurable effect on the mechanical properties of the material. Properties affected by grain size include hardness; strength; plasticity; fatigue resistance; and impact resistance [17].

This work aims to study and determine the influence of the geometrical parameters of the structural grains in the Ti–Al–C composites used in aviation on the mechanical properties of the material.

METHODS AND MATERIALS

Two series of samples, which were produced in different spark plasma sintering (SPS) regimes, were examined. The respective parameters of these regimes are presented in Table 2.

The selection and preparation of samples for metallographic analysis shall be following the ASTM E3 standard [18]. The recommended etching solutions and procedures are described in ASTM E407 [19]. The Ti–Al–C system test samples were etched with 186 etching agents according to ASTM E407. This solution is composed of 10 ml HF, 5l HNO_3, and 85 ml water. Sample etching time is 20 sec.

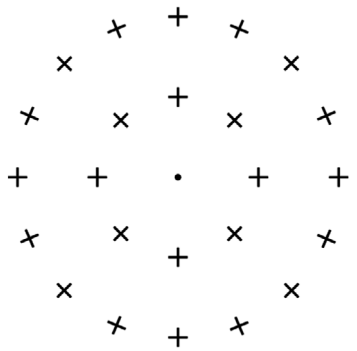

Fig. 4. An example of a grid [20]

TABLE 2. SPS Parameters for the Production of Samples

Series	*T*, °C	*I*, A	*t*, min	Approximate composition of the initial powder, %
G13	950	840	5	75 Ti, 15 Al_3Ti, 10 Ti_3AlC_2
13	985	995	5	75 Ti, 15 Al_3Ti, 10 Ti_3AlC_2

The ASTM E112 standard describes the methods for measuring grain size for single-phase materials. However, these methods can also be applied to multiphase materials by using the ASTM E562 [20] standard, which determines the fraction occupied by a component in the area under investigation. The geometric parameters of the grains are measured by the intersection method. The accuracy of grain size calculations for the intersection method is ±0.25 of grain size G, significantly better than the comparison method, which is ±1 of grain size G.

When performing measurements on multiphase materials, it is necessary to determine the fraction of the examined area occupied by the examined grains. This is done according to ASTM E562. This standard describes a systematic method of calculating and statistically estimating the fraction occupied by a given constituent. This method can be applied to any solid where the microstructure allows individual components to be identified. The method requires a grid of evenly spaced points. Grids can be square or circular. An example of such a grid is shown in Fig. 4. The grid is placed on the micrograph and calculations are performed. Grid points completely within the area occupied by the part are counted as 1 point, and points intersecting the grain only at boundaries are counted as 0.5 points. If it is not clear whether the point is inside or outside the grain, it is counted as 0.5 points. It is important to note that a point is considered the point of intersection of two lines, and not the entirety of the two lines. The number of zones to be calculated and the number of grid points can be selected according to Table 3. However, this is not mandatory.

The number of points within the boundaries of the component is determined by the following formula:

$$P_{pi} = \frac{P_i}{P_T} \cdot 100, \tag{1}$$

where P_{pi} is the percentage of points within the component *i* in that zone; P_i is the sum of the points within *i*-zone; P_T is the number of points in the grid used.

The arithmetic mean of the fraction of points within the component boundaries is given by (2):

$$\overline{P}_p = \frac{1}{n} \sum_{i=1}^{n} P_{pi}, \tag{2}$$

where $\overline{P}_p$ is the arithmetic mean of the fraction of points within the component boundaries; *n* is the number of zones.

TABLE 3. The Number of Calculated Zones Selected According to the Recommendations Based on the Desired Accuracy [20]

Volume fraction V_v, %	Number of required zones based on the number of points in the grid			
	16 points	25 points	49 points	100 points
	33% accuracy			
2	110	75	35	20
5	50	30	15	8
10	25	15	10	4
20	15	10	5	4
20% accuracy				
2	310	200	105	50
5	125	80	40	20
10	65	40	20	10
20	30	20	10	5
10% accuracy				
2	125	800	410	200
5	500	320	165	80
10	250	160	85	40
20	125	80	40	20

The obtained results are statistically processed according to formulas (3)–(6). The standard deviation is calculated according to the formula (3):

$$s = \left[\frac{1}{n-1} \sum_{i=1}^{n} \left[P_{pi} - \overline{P}_p \right]^2 \right]^{1/2}, \tag{3}$$

where s stands for standard deviation.

The 95% confidence interval (CI) is calculated according to formula (4):

$$\mathrm{CI}_{95\%} = \frac{t \cdot s}{\sqrt{n}}, \tag{4}$$

where t is a 95% confidence interval multiplier, which is chosen according to the standard [20].

The area occupied by the component is calculated according to the formula

$$V_v = \overline{P}_p \pm \mathrm{CI}_{95\%}, \tag{5}$$

where V_v is the area occupied by the component.

Finally, the relative accuracy (RA) is calculated according to formula (6):

$$\mathrm{RA} = \frac{\mathrm{CI}_{95\%}}{\overline{P}_p} \cdot 100. \tag{6}$$

The intersection method is recommended for microstructures where the grains do not have a regular shape. It can be performed using lines or circles. Procedures using circles have great advantages, which are:

- self-compensation for microstructures where grains are not regularly shaped; the linear method requires drawing of additional lines in different directions and calculating averages; when a circle is used, measurements are made in all directions;
- elimination of line end ambiguity.

The principle of the intersection method is simple: the length of the line or lines crossing the grains is divided by the number of grains crossed. The grain measurement procedure is based on this principle. Since the material under test is multiphase and the distribution of reinforcing particles is uneven, three concentric circles are used. The sequence of the process is as follows:

1. Three concentric circles are drawn, with their total length known.

2. After the count of the number of grains crossing the circumference of the circles, the average crossing length in the zone is calculated by the formula

$$\overline{\ell}_i = \frac{P_{pi} \cdot L_i}{N_i}, \tag{7}$$

where $\overline{\ell}_i$ is an average crossing length in zone *i*; L_i is the total length of the circles in zone *i*; N_i is a number of grains intersected by circles in zone *i*.

Statistical analysis is performed according to formulas (8)–(10).

The arithmetic mean of a crossing length is determined according to equation

$$\overline{\ell}_i = \frac{\sum \overline{\ell}_i}{n}, \tag{8}$$

where *n* is the number of measurements.

Next, the standard deviation is defined:

$$s = \left[\frac{\sum \left(\overline{\ell}_i - \overline{\ell} \right)^2}{n-1} \right]^{1/2}. \tag{9}$$

The confidence interval is calculated according to the previously used formula (4). Relative accuracy is calculated as follows:

$$\mathrm{RA} = \frac{\mathrm{CI}_{95\%}}{\overline{\ell}_i}. \tag{10}$$

3. Based on the source of [21], the geometrical parameters are determined (Table 4). According to the obtained average of the intercept length, the grain size *G* is determined.

ImageJ software is used to measure microstructured grains. This program is used for the drawing of concentric circles of known length in intersection procedures. Figure 5 shows a drawn circle in the microstructure, this figure also shows the area of the circle and other parameters.

ImageJ also has a point marking feature that automatically numbers the points. This eliminates the risk of losing numbers while counting. This function is illustrated in Fig. 6.

Finally, a grid function will be invoked, which will be used to calculate the area occupied by the component in the microstructure according to ASTM E562. The mesh in the microstructure is presented (Fig. 7). The grid density and number of points can be changed.

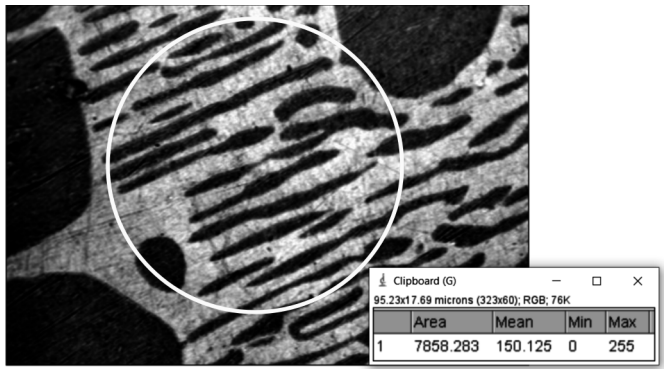

Fig. 5. Drawing a circle on a micrograph using ImageJ

TABLE 4. Grain Size Relationships Computed for Uniform, Randomly Oriented, and Equiaxed Grains

Grain size G	Number of grains (in a unit of area), N_A/mm^2	Average grain area, mm^2	Average grain diameter		Mean intercept, μm
			mm	μm	
00	3.88	0.2581	0.508	508	452.5
0	7.75	0.129	0.3592	359.2	320
0.5	10.96	0.0912	0.3021	302.1	269.1
1	15.5	0.0645	0.254	254	226.3
1.5	21.92	0.0456	0.2136	213.6	190.3
2	31	0.0323	0.1796	179.6	160
2.5	43.84	0.0228	0.151	151	134.5
3	62	0.0161	0.127	127	113.1
3.5	87.68	0.0114	0.1068	106.8	95.1
4	124	0.00806	0.0898	89.8	80
4.5	175.36	0.0057	0.0755	75.5	67.3
5	248	0.00403	0.0635	63.5	56.6
5.5	350.73	0.00285	0.0534	53.4	47.6
6	496	0.00202	0.0449	44.9	40
6.5	701.45	0.00143	0.0378	37.8	33.6
7	992	0.00101	0.0318	31.8	28.3
7.5	1402.9	0.00071	0.0267	26.7	23.8
8	1984	0.0005	0.0225	22.5	20
8.5	2805.8	0.00036	0.0189	18.9	16.8
9	3968	0.00025	0.0159	15.9	14.1
9.5	5611.6	0.00018	0.0133	13.3	11.9
10	7936	0.00013	0.0112	11.2	10
10.5	11223.2	0.000089	0.0094	9.4	8.4
11	15872	0.000063	0.0079	7.9	7.1
11.5	22446.4	0.000045	0.0067	6.7	5.9
12	31744.1	0.000032	0.0056	5.6	5
12.5	44892.9	0.000022	0.0047	4.7	4.2
13	63488.1	0.000016	0.004	4	3.5
13.5	89785.8	0.000011	0.0033	3.3	3
14	126976.3	0.000008	0.0028	2.8	2.5

Representative Volume Element (RVE) is the smallest volume that can be calculated to model a representative heterogeneous material from known homogeneous materials. RVE simulations are used to study porous materials, composites such as unidirectional carbon fibers or epoxy resins, and all anisotropic materials, that is,

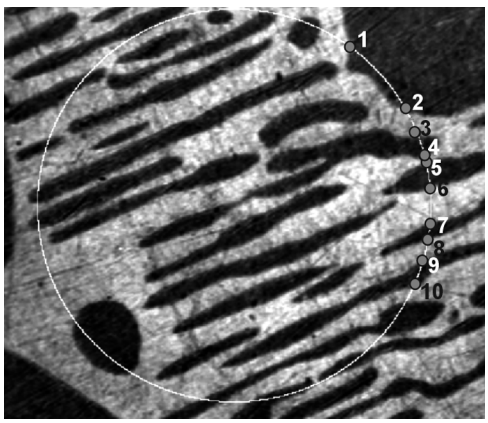

Fig. 6. Calculation using ImageJ

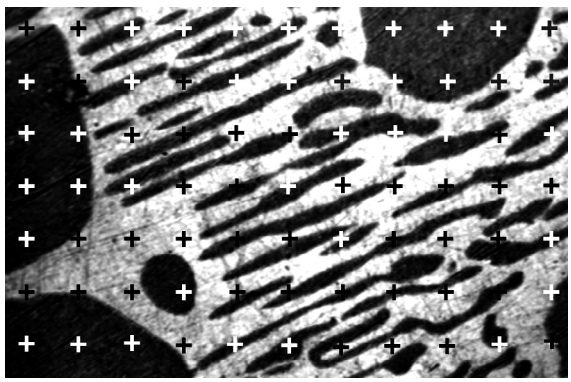

Fig. 7. Grid function in ImageJ program

materials whose mechanical properties vary in all directions. RVE simulation is a reliable method for studying anisotropic materials [22]. The amount, size, and distribution of reinforcing particles are critical parameters that define and determine the properties of the material [23]. The ANSYS Material Designer module will be used to perform the RVE study.

RESULTS AND DISCUSSION

Measurement of the Area Occupied by the Carbide Grains of Specimen G13.2 According to the ASTM E562 Standard. The number of grid points crossing carbide grains is counted. The calculations of the first micrograph are shown in Fig. 8. A grid of 100 points is selected. All points touching or within grain boundaries are marked in yellow (17 points), and only those points that only cross grain boundaries, or it is not clear whether they are inside or outside the grain (10 points) are marked in red. The number of points crossing grains in the *i*-th zone is calculated according to the formula below:

$$P_i = T_{vi} \frac{T_{ni}}{2}, \tag{11}$$

where P_i is the number of grid points crossing carbide grains in the *i*-zone; T_{vi} are points touching or within grain boundaries in the *i*-zone; T_{ni} are points that cross grain boundaries, or it is not clear whether they are inside or outside the grain in the *i*-zone.

The number of points crossing grains in zone 1 is calculated according to formula (11):

$$P_1 = 17 - \frac{10}{2} = 12 .$$

Because all micrographs of this specimen use a 100-point grid, P_i also shows the percentage of carbides. In this way, calculations are performed for the remaining micrographs/zones.

The percentage of points located within the component boundaries in the 1st zone is calculated using formula (1):

$$P_{p1} = \frac{12}{100} \cdot 100 = 12\% .$$

The calculations of the remaining micrographs are presented in Table 5.

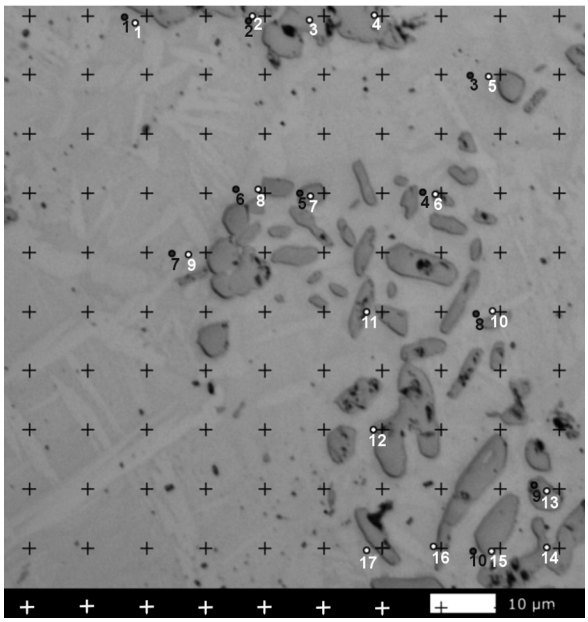

Fig. 8. Calculation of points crossing grains in zone 1 of specimen G13.2

TABLE 5. Measurement Results of the Area Occupied by Titanium Carbide Grains in the Micrographs of Sample G13.2

Zone	T_{vi}	T_{ni}	P_i	P_T	P_{pi}, %
1	17	10	12	100	12
2	21	13	14.5	100	14.5
3	24	15	16.5	100	16.5
4	22	11	16.5	100	16.5
5	26	13	19.5	100	19.5
6	41	19	31.5	100	31.5
7	20	7	16.5	100	16.5
8	32	15	24.5	100	24.5
9	41	21	30.5	100	30.5

The arithmetic mean of the fraction of points within the component boundaries is calculated according to formula (2):

$$\overline{P}_p = \frac{(12+14.5+16.5+16.5+19.5+31.5+16.5+24.5+30.5)}{9 \cdot 100} \cdot 100 = 20.22\% .$$

The obtained results are statistically processed following the methodology described above.

The Matlab std function is used to calculate the standard deviation: s = 7.014. The confidence interval is determined according to the formula (4):

$$\mathrm{CI}_{95\%} = \frac{2.306 \cdot 7.014}{\sqrt{9}} = 5.39 .$$

The area occupied by the component is calculated according to the formula (5):

$$V_v = 20.22\% \pm 5.39\% .$$

The relative accuracy is calculated using formula (6):

$$\%\mathrm{RA} = \frac{5.39}{20.22} \cdot 100 = 26.66\% .$$

The fraction occupied by titanium carbides in the microstructure is 20.22% with a relative error of 26.66%. This value will be used to determine the fraction occupied by TiC in the RVE model.

Study of Specimen G13.2 Determination of Mechanical Properties Using RVE Simulation. The RVE model is composed of a Ti–Al–C matrix (mainly of Ti, Al_4C_3, and Al_3Ti alloys [24]) and randomly distributed titanium carbide particles. The phase composition of the samples was determined in the previous work [24]. The MAX phase Ti_3AlC_2 was not detected, since its formation requires specific conditions, which depend on the temperature and carbon content [25].

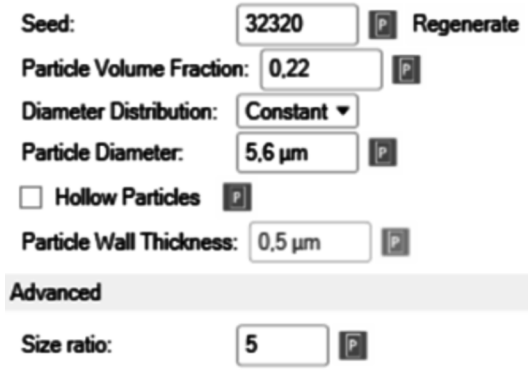

Fig. 9. Geometrical parameters of RVE model

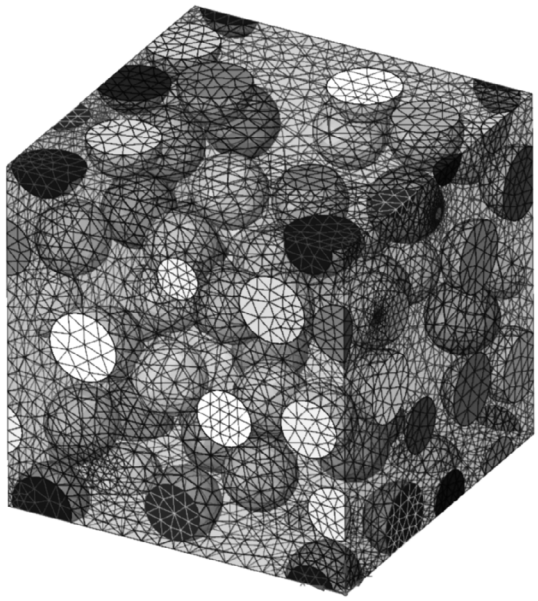

Fig. 10. Geometry and constructed mesh of specimen G13.2 RVE model

The fraction occupied by carbides in the model is recorded as 0.22, and the particle size is 5.6 μm. The size ratio of the geometry model is also recorded as 5 (Fig. 9). This parameter determines the ratio of the side of the cube to the length of the particles. According to this, it is known that the dimensions of the cube are 28 μm × × 28 μm × 28 μm. A mesh of 118,960 elements is created. The geometry of the RVE model and the generated grid are shown in Fig. 10.

The sequence of the simulation was as follows:

- the boundary conditions for the simulation were material properties, cube size, and load, which is constant;
- the constant load F was applied on the selected surface of a cube, A;
- the displacement L was obtained and used to calculate the deformation ε:

$$\varepsilon = \frac{L - L_0}{L_0}. \tag{12}$$

Elasticity modulus calculation:

$$E = \frac{F}{A} : \frac{L - L_0}{L_0} = \frac{F \cdot L_0}{A(L - L_0)}. \tag{13}$$

Poisson's ratio μ was obtained by determining the displacement in perpendicular direction and longitudinal one. The ratio of these values becomes Poisson's ratio.

Shear modulus is connected with elasticity modulus and Poisson's ratio:

$$G = \frac{E}{2(1 + 2\mu)}. \tag{14}$$

The simulation is performed at room temperature. Mechanical properties of the material were taken from the database of reference source [26], choosing the alloy with the closest elemental composition to the material we examined: modulus of elasticity is 116 GPa; Poisson's ratio ratio is 0.34.

Mechanical properties recorded for titanium carbides [27]: modulus of elasticity is 450 GPa; Poisson's ratio is 0.185.

The following calculations were performed based on load tests. According to the given geometry, loads are added and simulations are performed. The values obtained after performing the calculations: modulus of elasticity is 153.6 GPa; share modulus is 58.3 GPa; Poisson's ratio is 0.315.

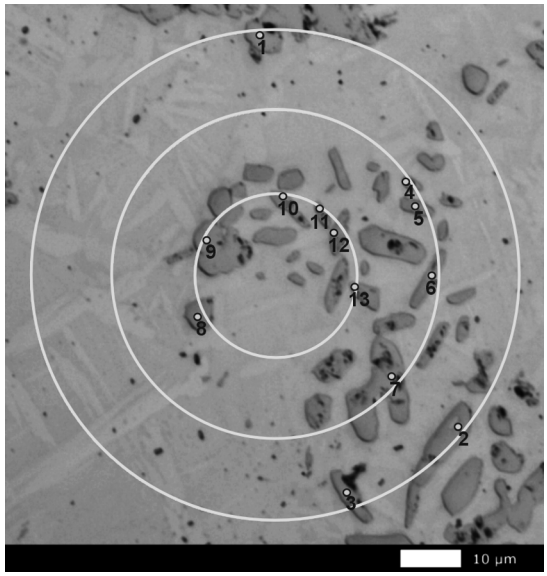

Fig. 11. Calculation of grains intersected by circles in zone 1 of sample G13.2

Measurement of the Geometrical Parameters of the Grains of Specimen G13.2 Using the Intersection Procedure. The calculation of the grains of specimen G13.2 intersected by circles using the intersection procedure is shown in the first micrograph in Fig. 11.

Calculations are made according to the methodology presented above. The average cross-sectional length in each zone is calculated as well. The value of the fraction occupied by TiC in the microstructure is that determined for the individual zone. The total length of the circles for all micrographs of sample G13.2 is 500 μm. The average cross-sectional length of the first micrograph is calculated according to equation (7):

$$\bar{\ell}_1 = \frac{0.12 \cdot 500}{13} = 4.62 \text{ μm}.$$

The average crossing length calculated for the remaining zones is presented in Table 6.

Statistical data processing is performed according to the previously described methodology. Arithmetic mean crossing length is found according to formula (8):

$$\bar{\ell}_1 = \frac{4.62 + 5.58 + 4.85 + 4.34 + 5.42 + 6.3 + 4.34 + 4.38 + 5.26}{9} = 5.01 \text{ μm}.$$

The function of the Matlab std is used to calculate the standard deviation: $s = 0.679$.

TABLE 6. Count of Grains Crossing Circles in Each Zone and Their Corresponding Calculated Mean Crossing Length for Specimen G13.2

Zone	N_i	P_{pi}	$\bar{\ell}_i$
1	13	12	4.62
2	13	14.5	5.58
3	17	16.5	4.85
4	19	16.5	4.34
5	18	19.5	5.42
6	25	31.5	6.30
7	19	16.5	4.34
8	28	24.5	4.38
9	29	30.5	5.26

Fig. 12. Calculation of points crossing grains in zone 1 of specimen 13.2

The confidence interval is calculated according to formula (4):

$$\mathrm{CI}_{95\%} = \frac{2.306 \cdot 0.679}{\sqrt{9}} = 0.52 .$$

The relative accuracy is calculated according to formula (10):

$$\mathrm{RA} = \frac{0.52}{5.01} \cdot 100 = 10.38\% .$$

The average crossing length of titanium carbides is calculated to be 5 μm with an error of 10.38%. According to Table 4, the average grain diameter is found to be 5.6 μm. This corresponds to a grain size of G12.

Measurement of the Area Occupied by the Carbide Grains of Specimen 13.2 According to the ASTM E562 Standard. The calculation of the points crossing the grains of sample 13.2 is shown in the first micrograph in Fig. 12.

The number of points crossing grains in zone 1 is calculated according to formula (11):

$$P_1 = 43 - \frac{24}{2} = 31.$$

The percentage of points located within the component boundaries in the 1st zone is calculated according to the formula (1):

$$P_{p1} = \frac{31}{225} \cdot 100 = 13.78\%.$$

In this way, calculations are performed for the remaining micrographs. These results are presented in Table 7.

The arithmetic mean of the fraction of points within the component boundaries is found according to formula (2):

$$\overline{P}_p = \frac{(13.78 + 22.22 + 19.33 + 14.44 + 18.5)}{5 \cdot 100} \cdot 100 = 17.65\% .$$

The std function of the Matlab program is used to calculate the standard deviation: s = 3.53.

The confidence interval is calculated according to formula (4):

$$\mathrm{CI}_{95\%} = \frac{t \cdot s}{\sqrt{n}} = \frac{2.776 \cdot 3.53}{\sqrt{5}} = 4.38 .$$

TABLE 7. Measurement Results of the Area Occupied by Titanium Carbide Grains of Sample 13.2

Zone	T_{vi}	T_{ni}	P_i	P_T	P_{pi}, %
1	43	24	31	225	13.78
2	63	26	50	225	22.22
3	54	21	43.5	225	19.33
4	46	27	32.5	225	14.44
5	26	15	18.5	100	18.5

The area occupied by the component is calculated according to the formula (5):

$$V_v = 17.65\% \pm 4.38\% .$$

The relative accuracy is calculated according to formula (6):

$$\mathrm{RA} = \frac{4.38}{17.65} \cdot 100 = 24.82\% .$$

The calculated area occupied by TiC particles in sample 13.2 is equal to 17.65% with a relative error of 24.82%. This value will be used to determine the fraction occupied by TiC in the RVE model.

Measurement of the Geometrical Parameters of the Grains of Specimen 13.2 Using the Intersection Procedure. The calculation of sample 13.2 grains intersected by circles in the 1st zone using the intersection procedure is shown in Fig. 13. The results of the calculations are presented in Table 7.

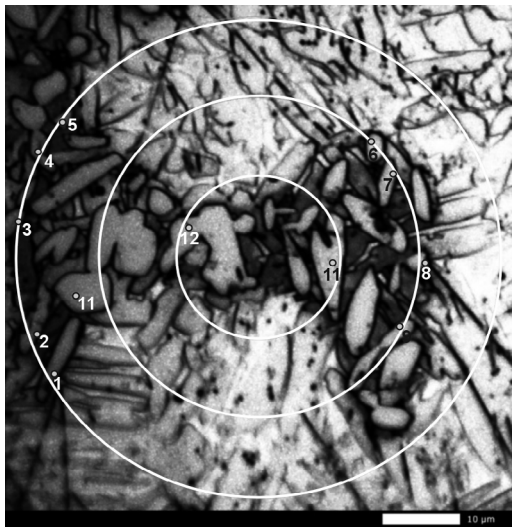

Fig. 13. Count of grains intersected by circles in zone 1 of specimen G13.2

TABLE 8. Counts of Specimen 13.2 Grains Crossing Circles in Each Zone and Their Corresponding Calculated Mean Crossing Length

Zone	N_i	P_{pi}, %	$\bar{\ell}_i$, µm	L, µm
1	12	13.78	4.48	390
2	16	22.22	5.42	390
3	19	19.33	3.97	390
4	15	14.44	3.76	390
5	32	18.5	3.06	530

The average crossing length of the TiC grains of the first micrograph is calculated according to the formula (7):

$$\bar{\ell}_1 = \frac{0.138 \cdot 390}{12} = 4.48 \text{ μm} .$$

The average crossing length calculated for the remaining zones is presented in Table 8.

Statistical data processing is performed according to the previously described methodology. Arithmetic mean crossing length is found according to formula (8):

$$\bar{\ell} = \frac{4.48 + 5.42 + 3.97 + 3.76 + 3.06}{5} = 4.14 \text{ μm} .$$

The std function of the Matlab program is used to calculate the standard deviation: $s = 0.87$.

The confidence interval is calculated according to formula (4):

$$\text{CI}_{95\%} = \frac{t \cdot s}{\sqrt{n}} = \frac{2.776 \cdot 0.87}{\sqrt{5}} = 1.08 .$$

The relative accuracy is calculated according to formula (10):

$$\text{RA} = \frac{\text{CI}_{95\%}}{\bar{\ell}} \cdot 100 = \frac{1.08}{4.14} \cdot 100 = 26.1\% .$$

The average crossing length of titanium carbides is calculated to be 4.14 μm with a relative error of 26.1%. According to Table 4, the average grain diameter is found to be about 4.7 μm. This corresponds to a grain size of G12.5.

Study of Specimen 13.2 Determination of Mechanical Properties Using RVE Simulation. The same RVE simulation as for specimen G13.2 is performed. The only difference is the TiC occupied area of 17.65% and grain diameter of 4.7 μm.

The geometry and mesh of the RVE model of specimen 13.2 are shown in Fig. 14.

Values obtained after performing calculations: modulus of elasticity is 145 GPa; shear modulus is 55.2 GPa; Poisson's ratio ratio is 0.319.

Comparison of the Mechanical Properties of the Modeled Composites with Each Other and with the Ti–6Al–4V Alloy. The mechanical properties of the modeled composites are compared with each other and with the widely used alloy Ti–6Al–4V in aviation. The elastic and shear moduli of materials, as well as Poisson's ratio, are compared. The properties of both composites are presented in Table 9.

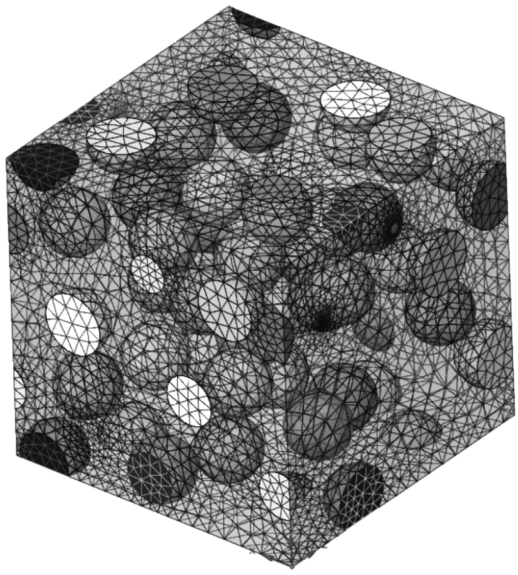

Fig. 14. The geometry and mesh of the RVE model of Specimen 13.2

TABLE 9. Comparison of the Mechanical Properties of the Modeled Composites with Each Other and with the Ti–6Al–4V Alloy

Materials to be compared	Modulus of elasticity, GPa	Shear modulus, GPa	Poisson's ratio
Specimen G13.2	153.6	58.3	0.315
Specimen 13.2	145	55.2	0.319
Ti–6Al–4V	113.8	44	0.342

It can be seen from the Table 9 that the simulated composites are stiffer due to higher Young's and shear moduli and lower Poisson's ratio values compared to the values of Ti–6Al–4V alloy [28]. Sample G13.2 is the stiffest of all the materials compared. It has a Young's modulus of 153.6 GPa, a shear modulus of 58.3 GPa, and a Poisson's ratio of 0.315. Sample 13.2 is less rigid. It has an elastic modulus of 145 GPa, a shear modulus of 55.2 GPa, and a Poisson's ratio of 0.319.

However, the difference between samples G13.2 and 13.2 is not significant because their geometric parameters differ only slightly. A higher concentration of TiC in the microstructure and larger grains resulted in higher stiffness properties.

CONCLUSIONS

The use of titanium, its composites, and alloys in aerospace is growing and will continue to grow. Titanium is most commonly used in airframe and engine applications. Titanium alloys and in particular Ti–Al–C system composites are promising materials for high-temperature applications. The use of Ti–Al–C system composites is currently limited by difficult manufacturing processes.

The methodology for studying the geometric parameters according to the microstructure preparation standard ASTM E3, etching standard ASTM E407, determining the area occupied by the component according to the standard ASTM E562, and measuring the geometric parameters according to the standard ASTM E112 is described.

The geometric parameters of samples G13.2 and 13.2 are similar. According to ASTM E112, they correspond to G12 and G12.5. The average diameter is 5.6 and 4.7 μm, respectively. According to ASTM E562, the occupied area of carbides was found to be 20.22 and 17.65% for samples G13.2 and 13.2, respectively.

Simulation results showed that material with larger average grain size and microstructure occupied area is stiffer. The Young's modulus of specimen G13.2 was 153.6 GPa, the shear modulus was 58.3 GPa, and the Poisson's ratio was 0.315. The Young's modulus of specimen 13.2 with lower concentration was 145 GPa, the shear modulus was 55.2 GPa, and the Poisson's ratio was 0.319. Both specimens tested are stiffer than the Ti–6Al–4V alloy widely used in aviation.

ARTICLE-LEVEL DECLARATIONS

Acknowledgments. The authors would like to express their gratitude to the Armed Forces of Ukraine for their bravery, which made this work possible even in the dark times of war.

Conflict of Interest. The authors declare that they have no known competing financial interests or personal relationships that could have appeared to influence the work reported in this paper.

Funding. The presented work was performed with partial financial support from the Research Council of Lithuania and the Ministry of Education and Science of Ukraine in the framework of "Application of high-concentrated energy flows for producing

and edited the final version.

Data Availability. Data will be made available on request.

REFERENCES

1. I. Masahiko, U. Masato, Y. Yusuke, *"*Developments of Cost Affordable Titanium Alloys in Japan*," Solid State Phenomena,* **353**, 115–120. doi: 10.4028/p-N1iiyW.
2. R. Boyer, *Titanium and Its Alloys: Metallurgy, Heat Treatment and Alloy Characteristics* (2010), ISBN 978-0-470-68665-2, https://doi.org/10.1002/9780470686652.eae198.
3. I. Inagaki, T. Takechi, Y. Shirai, and N. Ariyasu, "Application and features of titanium for the aerospace industry," *Nippon Steel & Sumitomo Metal Technical Report No. 106*, July, 22–27 (2014).
4. P. Singh, H. Pungotra, and N.S. Kalsi, "On the characteristics of titanium alloys for the aircraft applications," *Mater. Today: Proc.*, **4**, No. 8, 8971–8982 (2017), https://doi.org/10.1016/j.matpr.2017.07.249.
5. R. Gondaliya, D. Sypec, and Z. Feng, "Improving damage tolerance of composite sandwich structure subjected to low velocity Impact loading: Experimental analysis," in: *Conference: 31st American Society for Composites* (September, 2016), Williamsburg (2016), 1510 pp.
6. L. Li and Y. Chen, "The influence of sintering pressure on the preparation, friction properties, and magnetic properties of Ti_2AlC–TiC and Ti_3AlC_2–TiC composites under high-pressure and high-temperature," *Adv. Mater. Sci. Eng*., **2022**, Article ID 9108736 **(**2022), https://doi.org/10.1155/2022/9108736.
7. M. Yoshida, Y. Hoshiyama, J. Ommyoji, and A. Yamaguchi, "Reaction mechanism for the synthesis of Ti_3AlC_2 through an intermediate carbide of Ti_3AlC from elemental Ti, Al, and C powder mixture," *J. Ceram. Soc. Japan,* **118**, Issue 1373, 37–42 (2010), https://doi.org/10.2109/jcersj2.118.37.
8. X.H. Wang and Y.C. Zhou, "Layered machinable and electrically conductive Ti_2AlC and Ti_3AlC_2 ceramics: A review," *J. Mater. Sci. Technol.*, **26**, No. 5, 385–416 (2010), https://doi.org/10.1016/S1005-0302(10)60064-3.
9. L.J. Frodelius, *Thick and Thin Ti_2AlC Coatings. Linköping Studies in Science and Technology*, Dissertation No. 1328, 2010, ISBN: 978-91-7393-356-8. ISSN 0345-7524.
10. O. Syzonenko, E. Shregii, S. Prokhorenko, A. Torpakov, Ye. Lypian, V. Trehub, and B. Cieniek, "Electric discharge synthesis of titanium carbide," *Machines. Technol. Mater.*, **10**, No. 8, 34–37 (2016).
11. O. Syzonenko, Ye. Lypian, A. Torpakov, A. Zaichenko, and M. Prystash, "Effect of Al–Ti–C system master alloy high energy synthesis on efficiency of Ni based superalloy inoculation," *Machines. Technol. Mater.*, **13**, No. 8, 331–334 (2019).
12. O. Syzonenko, A. Torpakov, Y. Lypian, and M. Prystash, "The impact of high voltage electric discharge treatment on the properties of Cu–Al powder mixture," *Machines. Technol. Mater.*, **15**, No. 6, 248–251 (2021).
13. Y. Le Godec and S. Le Floch, "Recent developments of high-pressure spark plasma sintering: An overview of current applications, challenges and future directions," *Materials* **16**, No. 3, 997 (2023), https://doi.org/10.3390/ma16030997.
14. Z.W. Huang, P.L. Yong, H. Zhou, and Y.S. Li, "Grain size effect on deformation mechanisms and mechanical properties of titanium," *Mater. Sci. Eng.: A*, **773**, 138721 (2020), https://doi.org/10.1016/j.msea.2019.138721.
15. H. Garbacz, P. Wieciński, D. Kuczyńska, D. Kubacka, K.J. Kurzydłowski, "The effect of grain size on the surface properties of titanium grade 2 after different treatments," *Surf. Coat. Technol.*, **335**, 13–24 (2018), https://doi.org/10.1016/j.surfcoat.2017.12.005.
16. S. Benson, *Grain size. Part II: How Metal Grain Size Affects a Bending Operation [interactive]*, Access: https://www.thefabricator.com/thefabricator/article/bending/grain-size-part-ii-how-metal-grain-size-affects-a-bending-operation.
17. *Grain Size and Its Influence on Materials Properties. Industrial Heating: 2018, Heat Treating, Vol. 2 [interactive]*. Access: https://digital.bnpmedia.com/article/Grain+Size+And+Its+Influence+On+Materials+Properties/3214739/534828/article.html.

18. ASTM E3-11, *Standard Guide for Preparation of Metallographic Specimens* (2017).
19. ASTM E407-07el, *Standard Practice for Microetching Metals and Alloys* (2015).
20. ASTM E562-19el, *Standard Test Method for Determining Volume Fraction by Systematic Manual Point Count* (2020).
21. ASTM E112-13, *Standard Test Methods for Determining Average Grain Size* (2021).
22. P. Ferretti, G.M. Santi, Ch. Leon-Cardenas , E. Fusari, G. Donnici, and L. Frizziero, "Representative volume element (RVE) analysis for mechanical characterization of fused deposition modeled components," *Polymers,* **13**, No. 20, 3555 (2021), doi:10.3390/polym13203555.
23. Y. Cao, Representative volume element (RVE) finite-element analysis (FEA) of Al metal-matrix composites, *Theses and Dissertations* (2016), Access: https://dc.uwm.edu/etd/1256.
24. Rasa Kandrotaitė Janutienė, Darius Mažeika, Jaromír Dlouhý, Olha Syzonenko, Andrii Torpakov, Evgenii Lipian, and Arūnas Baltušnikas, "Investigation of the microstructure of sintered Ti–Al–C composite powder materials under high-voltage electrical discharge," *Materials*, **16**, No. 17, 5894 (2023), https://doi.org/10.3390/ma16175894.
25. Zahra Mahmoudia, Seyed Hadi Tabaiana, Hamid Reza Rezaieb, Farzad Mahboubia, and Mariyam Jameelah Ghazali, "Synthesis of Ti_2AlC & Ti_3AlC_2 MAX phases by Arc-PVD using Ti–Al target in C_2H_2/Ar gas mixture and subsequent annealing," *Ceram. Int.*, **46**, 4968 (2020), https://doi.org/10.1016/j.ceramint.2019.10.235.
26. *MatWeb. The Online Materials Information Resource [interactive]*. Access: https://www.matweb.com/errorUser.aspx?msgid=2&ckck=nocheck.
27. *Titanium Carbide, TiC [interactive]*. Access: https://www.matweb.com/search/datasheet_print.aspx?matguid=058d1b70edbd4b2293f298c52bbf9818.
28. *ASM Material Data Sheet. [interactive]*. Access: https://asm.matweb.com/search/SpecificMaterial.asp?bassnum=mtp641.